MATERIALS SCIENCE

A general approach to composites containing nonmetallic fillers and liquid gallium

Chunhui Wang[1], Yan Gong[1], Benjamin V. Cunning[1]*, Seunghwan Lee[2], Quan Le[1], Shalik R. Joshi[2], Onur Buyukcakir[1†], Hanyang Zhang[1], Won Kyung Seong[1], Ming Huang[1], Meihui Wang[1,3], Jaeseon Lee[2], Gun-Ho Kim[2], Rodney S. Ruoff[1,3,4,5]*

We report a versatile method to make liquid metal composites by vigorously mixing gallium (Ga) with non-metallic particles of graphene oxide (G-O), graphite, diamond, and silicon carbide that display either paste or putty-like behavior depending on the volume fraction. Unlike Ga, the putty-like mixtures can be kneaded and rolled on any surface without leaving residue. By changing temperature, these materials can be stiffened, softened, and, for the G-O–containing composite, even made porous. The gallium putty (GalP) containing reduced G-O (rG-O) has excellent electromagnetic interference shielding effectiveness. GalP with diamond filler has excellent thermal conductivity and heat transfer superior to a commercial liquid metal–based thermal paste. Composites can also be formed from eutectic alloys of Ga including Ga-In (EGaIn), Ga-Sn (EGaSn), and Ga-In-Sn (EGaInSn or Galinstan). The versatility of our approach allows a variety of fillers to be incorporated in liquid metals, potentially allowing filler-specific "fit for purpose" materials.

INTRODUCTION

Gallium (Ga) is an interesting material considering its various properties that include high electrical and moderate thermal conductivity and low toxicity in its liquid state (*1*–*3*). It is a promising ingredient for synthesizing intelligent functional materials (*4*) and can readily combine with many other metals to form low–melting point alloys (*5*–*7*). Three eutectic alloys of gallium indium (EGaIn), gallium tin (EGaSn), and gallium indium tin (EGaInSn or Galinstan) along with Ga are the most used gallium-based liquid materials (GLMs) (*1*–*4*).

GLMs have emerged as promising materials for the preparation of soft, flexible, and stretchable electronics in next-generation wearables, soft robots, and biocompatible devices (*8*–*12*); however, the surface tension of GLM tends to complicate its handling and processing and so presents challenges to patterning or reshaping (*13*). The inclusion of fillers to fabricate GLM-based composites is an effective method to solve these problems (*14*, *15*). GLM composites with improved thermal conductivity (*14*) or mechanical strength (*15*) have been fabricated.

Because Ga readily alloys, many different types of metallic particles can be wetted and intermetallic alloys can be made during mixing. Paste-like GLM mixtures including those with microparticles of Cu, Ag, or Mg were reported to be due to the formation of intermetallic compounds, namely, $CuGa_2$ (*15*), Ag_2Ga (*16*, *17*), and Mg_2Ga_5 (*18*). These intermetallic alloys formed during the mixing process will consume the Ga matrix, which will change the chemical composition of the liquid metal; this process occurs over a period of minutes to days, leading to the formation of solid intermetallic compounds and geometrical changes in the surface roughness (*15*–*17*). These studies are quite different from what we describe below.

Nonmetallic materials such as graphene, graphite, diamond, silicon carbide, and carbon nanotubes have outstanding thermal, electrical, or mechanical properties and are excellent fillers for the preparation of functional composite materials (*19*–*23*). Directly mixing nonmetallic fillers with GLM is reported to result in incomplete mixing or a very low loading (*24*, *25*). A third component such as metal particles or viscous polymers has been used to improve the dispersion. For example, pristine carbon nanotubes were reported to be nonmixable with EGaIn, but after being surface-functionalized with platinum particles, the loading mass was reported to increase to 15 weight % (wt %) (*24*). MXene particles could not be incorporated into pure liquid gallium but were reported to be dispersible when 1.9 atomic % of magnesium was added (*26*). In another approach, a chromium transition layer was deposited on the surfaces of diamond particles by magnetron sputtering, which facilitated dispersion with Ga (*27*). While these approaches can enable stable dispersions inside a GLM matrix, the introduction of a third medium changes the composition of the final composite and complicates the fabrication process. Innovative solutions to directly mix nonmetallic particles without an additional medium can lead to the filler remaining intact in the GLM, thereby producing new types of functional composites.

Recent studies have achieved promising results on the preparation of GLM composites without a third medium or intermetallic compounds. It was found that tungsten does not form room temperature intermetallic compounds with Ga but reportedly can still be incorporated with Ga or EGaInSn by mixing in oxygen-rich environments (*14*). These findings suggest that there is still much to learn about GLM composites.

We report a versatile method to incorporate various nonmetallic particles with GLM. By adjusting the particle size and making use of the Ga oxide layer on the GLM surface, nonmetallic particles can be dispersed in GLM, forming putty-like composites at high filler fractions. Soft and highly deformable Ga putty (GalP) with a high mass loading of graphene oxide (G-O), diamond (D), graphite (Gr), and silicon carbide (SiC) were fabricated by direct mixing. These GalPs

[1]Center for Multidimensional Carbon Materials (CMCM), Institute for Basic Science (IBS), Ulsan 44919, Republic of Korea. [2]School of Mechanical, Aerospace and Nuclear Engineering, Ulsan National Institute of Science and Technology (UNIST), Ulsan 44919, Republic of Korea. [3]Department of Chemistry, Ulsan National Institute of Science and Technology (UNIST), Ulsan 44919, Republic of Korea. [4]Department of Materials Science and Engineering, Ulsan National Institute of Science and Technology (UNIST), Ulsan 44919, Republic of Korea. [5]School of Energy and Chemical Engineering, Ulsan National Institute of Science and Technology (UNIST), Ulsan 44919, Republic of Korea.
*Corresponding author. Email: rsruoff@ibs.re.kr, ruofflab@gmail.com (R.S.R.); ben.cunning@gmail.com (B.V.C.)
†Present address: Department of Chemistry, Izmir Institute of Technology, 35430 Urla, Izmir, Turkey.

could be kneaded and rolled on a surface without leaving dark stains on the surface. The filler X plays an important role on the performance of GalP (X). By changing its temperature, GalP (G-O) can become porous (T > 200°C) due to the gas release from G-O that yields reduced G-O (rG-O). This porous foam was able to return to a viscous GalP (rG-O) putty by grinding. GalP (rG-O) showed excellent electromagnetic interference (EMI) and ultraviolet (UV) shielding effectiveness (SE) when used as a coating. A GalP (rG-O) sheet with high thermal conductivity up to 126 ± 3.1 W m^{-1} K^{-1} parallel to the sheet showed outstanding heat transfer property as thermal interface material (TIM) matching the performance of a commercial liquid metal–based paste, indicating the multifunctionality of GalP (rG-O). GalP [diamond (D)] proved even better, exceeding the performance of the commercial thermal paste. We could also make EGaIn, EGaSn, and EGaInSn (Galinstan) putty by our method.

RESULTS AND DISCUSSION

Here, we primarily focus on the formation of GalP (G-O), but this methodology can be used to form other GalP composites with nonmetallic fillers, and these are detailed in the Supplementary Materials. One of the key factors we found in filler mixability was the particle size. For G-O, an average flake lateral dimension of >10 μm was necessary to form a stable GalP. For other fillers, we also found similar size-dependent behavior in forming a stable GalP. For example, GalP (SiC) could not be made with 0.5-μm SiC particles, but a stable GalP could be made when the particle size was increased to ~102 μm. As shown in Fig. 1A, GalP (G-O) could be kneaded (movie S1) and rolled on glass or metal surfaces (fig. S1) without leaving a residue. Two pieces of GalP (G-O) can be fused by bringing them into contact followed by gentle compression (fig. S1), indicating that this putty-like phase is a highly versatile form of Ga.

In a typical GalP (G-O) preparation experiment, liquid Ga was added to a Teflon beaker by a plastic syringe or dropper and heated to 40°C (because Ga highly wets silicate glass and readily forms alloys with most metals, we only used plastic labware in the preparation). Next, small portions of G-O powder were gradually added under vigorous mechanical stirring. The transition from a nonviscous liquid dispersion to putty-like behavior was characterized by both a substantial rise in viscosity and the absence of flow unless physically agitated [i.e., GalP (G-O) exhibits a yield stress]. A substantial increase in viscosity was observed when the G-O loading exceeded 1.6 wt %, and when it exceeded 1.8 wt %, the liquid turned into a highly viscous "paste-like" mixture as illustrated by a sample in a tilted beaker (fig. S2). At this point, the high viscosity prohibited further mechanical mixing. At 1.8 wt % loading, GalP (G-O) behaved like a putty: This was the threshold loading to make this type of putty. Further incorporation of G-O could be achieved by transferring the mixture to an oscillating ball mill with additional G-O. A maximum of 8.0 wt % could be incorporated in this manner, but above 5.0 wt % GalP (G-O), the material had a texture similar to partially dried clay (fig. S2)—cracks were seen on the surface. As noted above, the tensile mechanical strength of GalP (G-O) began to drop for loadings higher than 3.6 wt %. Unless otherwise stated, all GalP (G-O) preparations in this study have a composition of 3.6 wt %.

GalP (G-O) is highly processable and versatile, and it can be easily formed into various shapes (Fig. 1B). Various macroscopic shapes (rods, films, or bulk blocks) were easily prepared by common methods including cutting, molding, and carving (figs. S3 and S4). In addition, it showed different behaviors at different temperatures. Above the GalP (G-O) melting point (T = 31.9°C; fig. S5), it could be easily deformed or cut (in general, holding it in the hand retains the soft state) and "frozen" to a stiff solid that retained its shape when the temperature was below 31.9°C (Fig. 1C). As shown in Fig. 1C, a 5-g piece of soft GalP (G-O) can be sliced easily when T > 31.9°C but, when cooled and hardened, can support a 500-g steel block. Furthermore, liquid Ga undergoes a volume expansion of 3.2% when it solidifies (*1*–*3*), resulting in pure solid Ga samples having a "bulging" surface, but we observe no such expansion during GalP (G-O) solidification, allowing the fabrication of solid samples with precise shapes from the putty phase (fig. S6). We attribute this to the presence of some internal porosity in GalP (G-O) that provides internal volume for the gallium to "expand into" upon solidification.

To determine the nature of the interaction between Ga and G-O, we imaged GalP (G-O) by scanning electron microscopy (SEM) and transmission electron microscopy (TEM). Low-magnification SEM imaging (Fig. 1D) revealed a network of G-O sheets embedded in a matrix of Ga. The G-O sheets aggregated, and some pores formed due to the way G-O was incorporated into Ga. High-magnification SEM (Fig. 1E) and TEM (Fig. 1F) images showed that the G-O sheets were covered with Ga (fig. S7). In aqueous solutions, oxygen-containing (hydroxyl, carboxyl, and epoxy) functional groups on the G-O surface allow extensive hydrogen bonding, which results in a high degree of dispersion (single layers at low concentrations) (*28*). No such functional groups exist in Ga to assist the G-O dispersion, and thus, we see agglomeration of G-O (fig. S8) to form a network throughout Ga (Fig. 1D), with a percolation threshold at 1.8 wt %, as calculated from the viscosity data (Fig. 1G), which is much higher than typical percolation thresholds observed in well-dispersed G-O composites (*29*). The density of GalP (G-O) ranges from 3.0 to 4.1 g cm^{-3}, depending on the G-O loading (Fig. 1H). The highest tensile strength of solid GalP (G-O) at room temperature was 38.3 MPa (at 3.6 wt % G-O), which is 2.5× that of pure Ga at room temperature (Fig. 1I and fig. S9). The compressive strength also increased 3.2× compared to pure Ga (Fig. 1I and fig. S9). The increase in strength values over the pure liquid metal of our composite is comparable to those reported for a composite of EGaIn containing 15 wt % Pt-decorated carbon nanotubes (*24*) that were used to three-dimensionally (3D) print interconnects, suggesting that GalP (G-O) will also serve well in this application. In addition, the exceptional EMI shielding and thermal conductivity of GalP putties could be very useful in certain types of 3D printed structures.

We attempted to form GalP (G-O) using G-O with smaller average flake diameters (<10 μm); however, we found that these smaller flakes were wrapped by a Ga_2O_3 layer and floated on the Ga surface after mixing. A similar size-dependent behavior was observed when we attempted to make GalPs with other nonmetallic fillers (fig. S10). GalP (SiC) was successfully formed when the particle size was 102 μm, but it was not possible with a 0.5-μm particle size. Likewise, GalP (Gr) could be formed with a particle size of 180 μm, but not with 77 μm. For GalP (D), the commercial availability of diamond powder with different particle size distributions allowed us to determine the size cutoff between mixable and nonmixable more accurately (fig. S11). Diamond advertised as 4 to 8 μm in range was mixable; however, the 0- to 6-μm range product was nonmixable (average particle sizes of 6.5 and 5.5 μm, respectively). When the filler particle size is too small to form GalP, the particles became "nonmixable" and formed a separate phase with a Ga_2O_3 layer (fig. S12), suggesting that apart

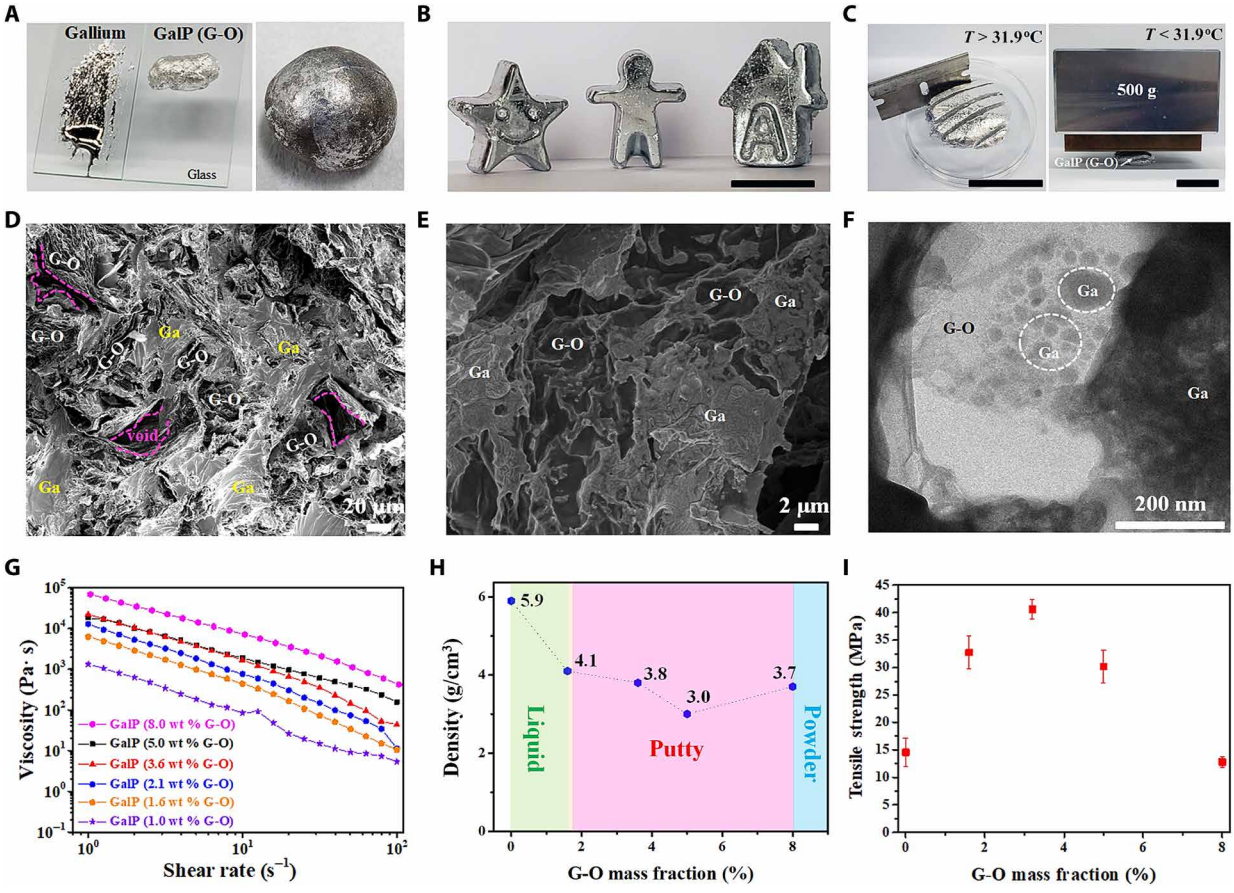

Fig. 1. Synthesis and characterization of a metallic putty made from liquid gallium with a graphene oxide filler. (**A**) Left photo shows liquid gallium and GaIP (G-O) (3.6 wt % G-O) on glass slides; right photo shows a GaIP (G-O) (8.0 wt % G-O) ball with some brown regions on its surface due to the high G-O loading—this GaIP (G-O) is easy to crack. (**B**) GaIP (G-O) is highly processable and versatile; it can be readily reshaped to a five-pointed star, a figurine, and a house. Scale bar, 2 cm. (**C**) Photos showing that GaIP (G-O) can be either soft or stiff depending on the temperature: A 5-g piece of soft GaIP (G-O) can be sliced easily when $T > 31.9$°C (left), and the slice can support a 500-g steel block when $T < 31.9$°C (right). Scale bars, 2 cm. (**D**) SEM image of GaIP (G-O); pink dotted lines indicate some pores generated by the stacking of the G-O sheets. (**E**) Magnified SEM image and (**F**) TEM image showing the combination of a G-O sheet with gallium. (**G**) Viscosity of GaIP (G-O) (with different G-O mass loading) under different shear rates. (**H**) Density of GaIP (G-O) as a function of the G-O mass fraction. (**I**) Tensile strength of GaIP (G-O) with different G-O mass fractions. Photos in (A) and (B) were taken at 26°C, and Ga in (A) is liquid due to supercooling. Photo credits: Chunhui Wang, Center for Multidimensional Carbon Materials, Institute for Basic Science.

from the particle size, the "particle–Ga_2O_3 layer–bulk Ga" interaction could be important in the successful formation of a putty-like phase.

Upon exposure to air, Ga and its alloys spontaneously form a ~1- to 3-nm-thick oxide layer (*30*–*34*) composed of Ga_2O_3 (figs. S12 and S13), which is akin to the protective coating of aluminum oxide on metallic aluminum (*35*). However, the formation of this layer is suppressed at sufficiently low levels of oxygen [<1 part per million (ppm)] (*7*). To investigate the role of the Ga oxide layer in the formation of GaIP (G-O), we attempted to mix G-O and Ga in an environment free of oxygen and water (<0.5 ppm) inside an inert atmosphere (Ar) glove box. We found that under these conditions, G-O (and other particles) could not be incorporated in Ga at any concentration. When this same mixture was removed from the glove box, G-O could then be easily incorporated by stirring to form GaIP (G-O), thus demonstrating that oxygen, and, in turn, Ga_2O_3, is critical for mixing and the subsequent putty phase to form. This behavior was true for all fillers that we could successfully form into GaIP. Previous reports have suggested that the Ga_2O_3 skin of GLMs can behave as surfactants (*36*) lowering the interfacial tension of GLMs with electrolytes. This behavior could be responsible for the incorporation of filler particles during mixing, allowing a stable filler–gallium oxide–gallium metal interaction that can only form in the presence of air. The particle shape of G-O made cross-sectional TEM imaging of the particle-Ga interface difficult, but imaging and elemental mapping of the particle-filler interface in GaIP (D) is suggestive of each filler particle being coated by a thin gallium oxide skin (figs. S14 and S15).

There are a number of recent reports demonstrating that the wetting behavior of liquid Ga on a surface is highly dependent on roughness rather than surface chemistry due to the presence of the Ga oxide skin (*37*–*39*), and our own experiments on particle mixing followed this behavior. Agglomerations of smaller-sized particles create a surface of higher effective roughness compared to larger-sized particles, and thus, smaller particles are nonwettable. Instead, agglomerations of small particles, and perhaps individual particles, are covered by a weakly interacting and nonconformal oxide coating and remain nonmixable in liquid Ga (Fig. 2, A and B). Furthermore, we could not mix large particles when they had hierarchical surface features; mesoporous silica and activated alumina with particle sizes up to 200 μm were nonmixable; however, regular, nonporous powdered silica is mixable. We

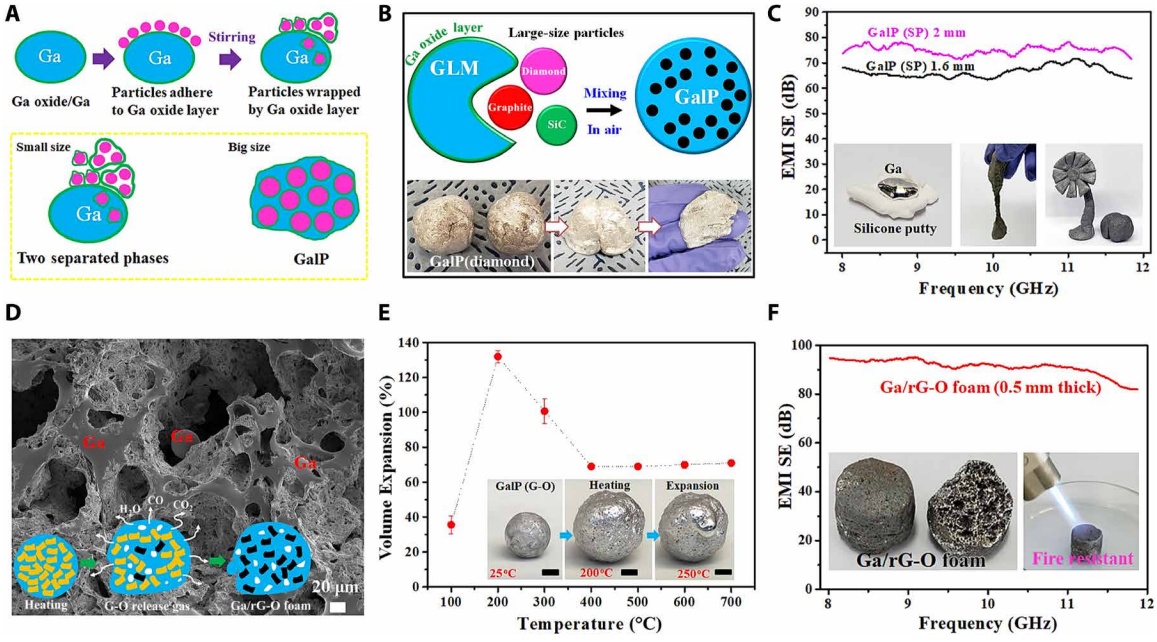

Fig. 2. Fabrication of various nonmetallic/GLM composites and a porous Ga/rG-O foam. (**A**) Illustration of the formation mechanism of GaIP; the particle size and Ga oxide layer are two key factors in the formation of GaIP. (**B**) Illustration showing the fabrication of GLM composites by mixing graphite flakes, diamond, or SiC particles with GLM; as long as the particle size is large enough, it is able to be incorporated with GLM. (**C**) EMI SE of a GaIP (SP) composite with thicknesses of 1.6 and 2.0 mm. Inset: Photos showing that GaIP (SP) is stretchable. (**D**) SEM image of a porous Ga/rG-O foam. Inset: Illustration showing the volume expansion of GaIP (G-O); the blue background represents the Ga matrix, the yellow sheets represent G-O, the black sheets represent rG-O, and the white dots are the pores formed. (**E**) Volume expansion of GaIP (G-O) with different G-O mass loadings as a function of temperature. Inset: Optical photos showing the volume expansion of a GaIP (G-O) (3.6 wt % G-O) ball upon heating. Scale bars, 2.0 cm. (**F**) EMI SE of porous Ga/rG-O foam with a thickness of 0.5 mm. Inset: Left photo shows the exterior and interior of a Ga/rG-O foam; right photo shows that the Ga/rG-O foam is heat resistant, as it remains stable under a blowtorch. Photos in (B) and (C) were taken at 26°C. GaIP (D) and GaIP (SP) are soft due to being handheld. Photo credits: Chunhui Wang, Center for Multidimensional Carbon Materials, Institute for Basic Science.

thus propose that fillers above a critical size and also lacking surface micro- or nano-texture are mixable.

It has been observed that when the volume of liquid gallium is small, the behavior of the oxide skin dominates the rheological properties (*5*, *40*), showing viscoelastic behavior with a high yield stress (*41*). We thus propose that GaIPs form as shown schematically in figs. S16 and S17. During mechanical stirring, particles are gradually dragged into the liquid Ga with the Ga oxide, and then a new oxidation layer is formed on the Ga surface (but is suppressed in oxygen-free environment). This process continues until the percolation threshold is reached and a continuous network is formed within the Ga matrix. The continual incorporation of fillers encapsulated by gallium oxide skin into the interior of the bulk increases viscosity due to standard melt-filler behavior (*42*). However, as the filler volume increases, the GaIP bulk is better described as an interconnected network of liquid gallium and its associated oxide skin between filler particles at length scales where the viscoelastic gallium-skin behavior dominates (see particle-particle distances in fig. S17B). Thus, we suggest that our observed paste and putty-like behaviors are a result of the combination of increased viscosity and skin-induced viscoelasticity. This putty-like behavior was also observed when eutectic GLMs (EGaIn, EGaSn, and Galinstan) were mixed with nonmetallic particles, and the formation of these composites followed the same behavior as observed with pure Ga (figs. S18 and S19). This is likely due to the same filler-melt behavior and gallium oxide surface skins on Ga eutectic metals (*41*, *42*). The as-prepared eutectic GaIP had a similar processability to the putty made with pure Ga.

Note that directly mixing Ga with a commercial silicone putty ["silly putty" (SP); Crayola LLC] is another way to obtain a malleable Ga composite, as shown in Fig. 2C, although it has a different combination mechanism in which Ga was dispersed as micrometer droplets in the SP. This GaIP (SP) was not only kneadable but also stretchable because of the polymer matrix. We tested GaIP (SP) as an instant patch for EMI shielding, and it showed excellent performance (Fig. 2C).

The possible uses and performance of GaIP are largely determined by its filler. GaIP (G-O) can be used as a precursor to fabricate a free-standing and porous (not putty-like) Ga/rG-O foam. The thermal deoxygenation of G-O proceeds with a substantial gas release (*43*) so that G-O acts as a "blowing agent," resulting in a free-standing foam-like structure (Fig. 2D, fig. S20, and movies S2 and S3). The pore sizes in the foam ranged from 5 to 100 μm, and thermogravimetric analysis coupled with mass spectrometry (TGA-MS) results showed that gaseous species (water molecules, carbon monoxide, and carbon dioxide) were generated during the thermal expansion by the reduction (that is, deoxygenation) of G-O and the elimination of interlamellar H_2O between stacked G-O sheets (fig. S21). This gas evolution produced porosity in GaIP, but the high viscosity prevented the pores from collapsing, resulting in a large volume expansion. We observed substantial expansion of GaIP (G-O) from 100° to 200°C, but above 200°C, some liquid Ga "escaped" from the sample and appeared in the form of droplets on the composite surface (Fig. 2E, inset). With further heating, more liquid gallium separated, and the composite volume decreased from 200° to 400°C but remained

unchanged in the temperature range of 400° to 700°C. When $T > 700$°C, rG-O completely separated from Ga (fig. S22). The free-standing Ga/rG-O foams discussed later were prepared by heating GalP (G-O) at 700°C for 1 hour.

The Ga/rG-O foam has high thermal stability. We evaluated its fire resistance by subjecting it to a blowtorch flame for 1 min (Fig. 2F, inset). After this, it remained intact without any structural change or degradation. The Ga/rG-O foam has a compressive strength of 0.4 MPa at room temperature (as compared to, e.g., 2.8 MPa for aluminum foam) (*44*). We found this Ga/rG-O foam to be an excellent candidate for EMI shielding. A sheet with a thickness of 0.5 mm showed extraordinary EMI SE, up to 90 dB at 8.2 GHz, enough to block 99.9999999% of incident radiation. At present, metals are excellent candidates to shield from EM waves because of their high electrical conductivity (*45*). In the Ga/rG-O foam, Ga is responsible for the high electrical conductivity, which is beneficial for reflecting radiation using charge carriers that interact directly with the EM fields. The rG-O content makes the composite freestanding, lightweight, and thermally stable, which broadens its range of applications.

We attempted to mix rG-O powder directly with Ga, but two separate phases were formed due to the small rG-O flake diameter (<10 μm). However, we found that it is possible to turn the Ga/rG-O foam into a putty-like form, by grinding it in Ga at 50°C (fig. S22). GalP (rG-O) made in this way contains 1.6 wt % rG-O and has a tensile strength of 34.4 MPa (fig. S22) at room temperature.

GalP (rG-O) can also be used as an effective EMI shielding coating. Shielding material thickness is critical in EMI SE, and as electronic devices are miniaturizing, the shielding materials must be adapted to smaller sizes. GalP (rG-O) coatings with different thicknesses were readily coated on any substrate by a blade, and the coating was highly effective for EMI and UV shielding (fig. S23). For example, after coating with 1-μm-thick GalP (rG-O), 100-μm-thick transparent films made from glass, cellulose nanofibers (CNFs), and polyethylene terephthalate (PET) had negligible transmission in the wavelength range of 280 to 400 nm, indicating almost complete shielding of UV rays in both the UV-A and UV-B regions (Fig. 3A).

By applying a thin layer of GalP (rG-O), common materials such as A4 paper could be turned into EMI shielding materials (figs. S23 and S24). A4 paper coated with a 10-μm-thick layer of GalP (rG-O) has an SE of more than 40 dB in the X-band (Fig. 3B), satisfying commercial requirements (>30 dB) (*45*). When the thickness was increased to 20 μm, the EMI SE was more than 70 dB in the X-band, which satisfies military shielding requirements (>60 dB) (*45*). The highest EMI SE value, 78 dB, was achieved for GalP (rG-O) coatings ≥40 μm on A4 paper, which blocked 99.99999% of the incident radiation in the X-band.

Electrically conducting graphene films made from rG-O (see Materials and Methods) were also tested as substrates for the GalP (rG-O) coating. Cross-sectional SEM images of the rG-O/GalP (rG-O) film showed a conformal interface between the two layers with no gaps or voids (Fig. 3C). The composite film could be folded or rolled without delamination (Fig. 3C) and had a tensile strength of 59.5 MPa at room temperature (Fig. 3D). The GalP (rG-O) coating maintained its integrity with the rG-O film even when subjected to temperatures as high as 700°C. To highlight the stability of the composite film, a piece was immersed in ethanol and ignited. Even after burning, GalP (rG-O) was still firmly attached to the rG-O film (Fig. 3D, inset). Pure rG-O films (17.2 and 30.0 μm thick) show an EMI SE less than 20 dB in the X-band. However, after coating with 3.5 μm of GalP (rG-O), the EMI SE of a 17.2-μm-thick rG-O film increased from 16 to 65 dB at 8.3 GHz and improved to 75 dB when the GalP (rG-O) thickness was 13.0 μm (Fig. 3E). The specific EMI shielding effectiveness (SSE) is used to evaluate different materials by accounting for the material's density. However, SSE alone is not a sufficient parameter for comparing practical SE, as a higher shielding efficiency can be achieved by making a thicker (but heavier) sample. Therefore, a more useful parameter is to divide SSE by the material thickness (SSE/*t*) (*46*). The rG-O/GalP (rG-O) (17.2 μm/3.5 μm; t = 20.7 μm) film gives an SSE/*t* of 24,800 dB cm^2 g^{-1} at 8.3 GHz, several to many times higher than metal foils and carbon films (table S1).

Shielding (at 8.0 GHz) from absorption (SE_A) and reflection (SE_R) in rG-O (30.0 μm) and rG-O/GalP (rG-O) (17.2 μm /13.0 μm) films is plotted in Fig. 3F. Shielding due to absorption was the dominant mechanism of rG-O/GalP (rG-O) because of the high electrical conductivity of GalP (rG-O). When EM waves reach the surface of GalP (rG-O), most are immediately reflected due to the abundance of free electrons from Ga in GalP (rG-O) (fig. S23A). The remaining waves enter the GalP (rG-O) layer, and a fraction is dissipated as heat by the Joule effect. Any radiation still remaining then reaches the rG-O film, which also acts as a reflecting and adsorption base. The combination of the two films also gives rise to multiple internal reflections at their interface. The EM waves reflect back and forth between the layers until they are completely absorbed and thus dissipated in the form of heat. These data indicate that GalP has the potential for use as a new material in EMI shielding. The superb heat spreading ability of GalP (rG-O) (its very high in-plane thermal conductivity) should allow the absorption of high intensity radiation without thermal damage.

The thermal conductivity (κ) of GalP (rG-O) was measured in part because it contributes to the heat dissipation when used as an EMI shielding coating. For testing, it was made into a circular sheet with a thickness of 1.0 mm and a diameter of 25.0 mm. GalP (rG-O) has a κ of 10.5 ± 2.3 W m^{-1} K^{-1} perpendicular to the sheet (Fig. 4A), which is much higher than values for traditional polymer-based thermal greases (<5 W m^{-1} K^{-1}). Because of the anisotropy of rG-O and the tendency of the sheets to align during doctor blading, the GalP (rG-O) sample has a high κ of 126 ± 3.1 W m^{-1} K^{-1} parallel to the sheet.

We also tested the thermal performance of GalP (D) with differently sized diamond particles. For diamond composites, a general trend has been reported in which larger diamond particle sizes have higher thermal conductivities (*47*), which we also observed in GalP (D) (fig. S25). GalP (D) made with a particle size of 250 μm had excellent thermal conductivity both perpendicular (104.5 ± 2.7 W m^{-1} K^{-1}) and parallel (116.9 ± 3.8 W m^{-1} K^{-1}) to the sheet, as shown in Fig. 4A. A comparison of the heat transfer between GalP (rG-O) and GalP (D) is shown in Fig. 4B. Samples of each material (1.0 cm × 1.0 cm × 0.5 cm) were placed on a hot plate at room temperature and then heated together while being monitored by a calibrated infrared (IR) camera to record their time-dependent surface temperature. The results in Fig. 4B show that the surface temperature of GalP (D) increases much faster than that of GalP (rG-O), indicating faster heat transfer through the thickness of the sheet.

The high malleability of prepared GalPs allows them to effectively conform to surface roughness (Fig. 4C), giving them the potential for use as a TIM. To investigate the heat transfer performance of GalP in a "real-world" environment, a system was built to test the capability of GalPs (rG-O or D) to act as a TIM (Fig. 4C). GalP samples

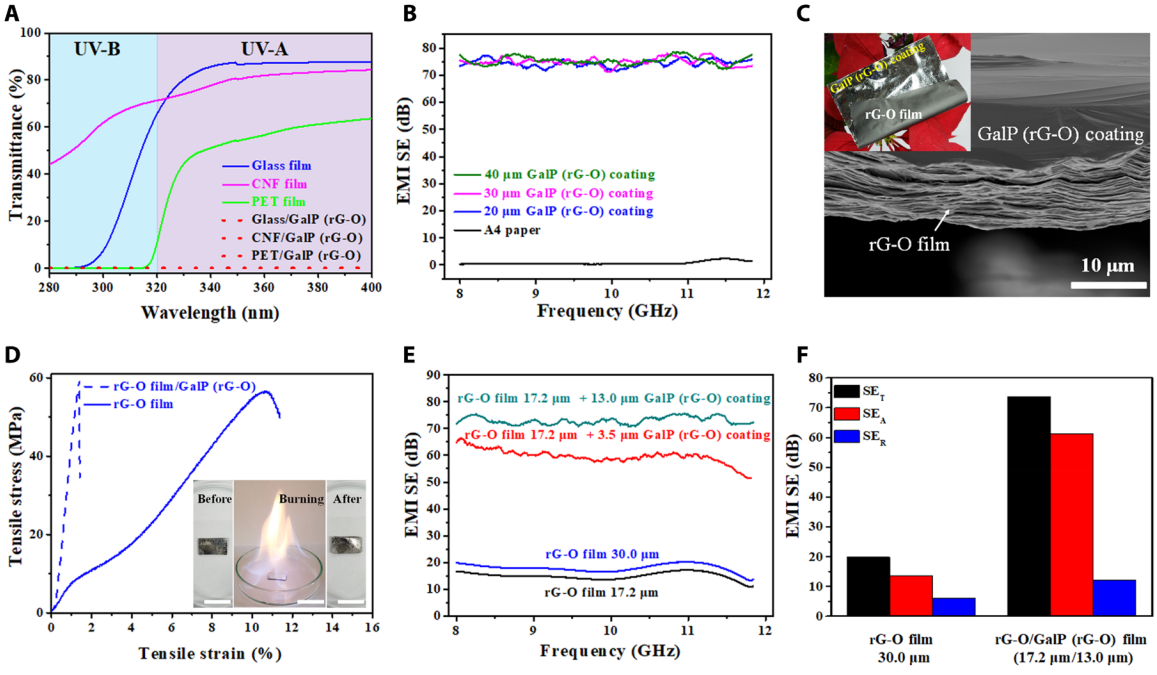

Fig. 3. GaIP on various substrates as a UV or electromagnetic shielding coating. (**A**) UV-vis spectra of glass/GaIP (rG-O), CNF/GaIP (rG-O), and PET/GaIP (rG-O) film. The transparent glass, CNF, and PET films exhibit complete shielding of UV rays in both the UV-B and UV-A regions, after coating with 1-μm-thick GaIP (rG-O) coating. (**B**) EMI SE of GaIP (rG-O) of different thicknesses coated on a commercial A4 paper. (**C**) SEM image of the cross section of an rG-O/GaIP (rG-O) film. Inset: Photo showing the rG-O film with a GaIP (rG-O) coating; the composite film is highly flexible and can be rolled up. (**D**) Tensile strain-stress curves of a rG-O and rG-O/GaIP (rG-O) film. Inset: The GaIP (rG-O) coating is heat-resistant and has a strong adhesion to the rG-O film; a piece of rG-O/GaIP (rG-O) composite film remains unchanged after being burned in an alcohol solution in air. (**E**) EMI SE of rG-O films at a thickness of 17.2 and 30.0 μm, and 17.2-μm-thick rG-O films with 3.5- and 13.0-μm-thick GaIP (rG-O) coatings. (**F**) Total EMI SE (EMI SE_T) and its absorption (SE_A) and reflection (SE_R) components in ~30.0-μm-thick rG-O film and rG-O/GaIP (rG-O) film at 8.0 GHz.

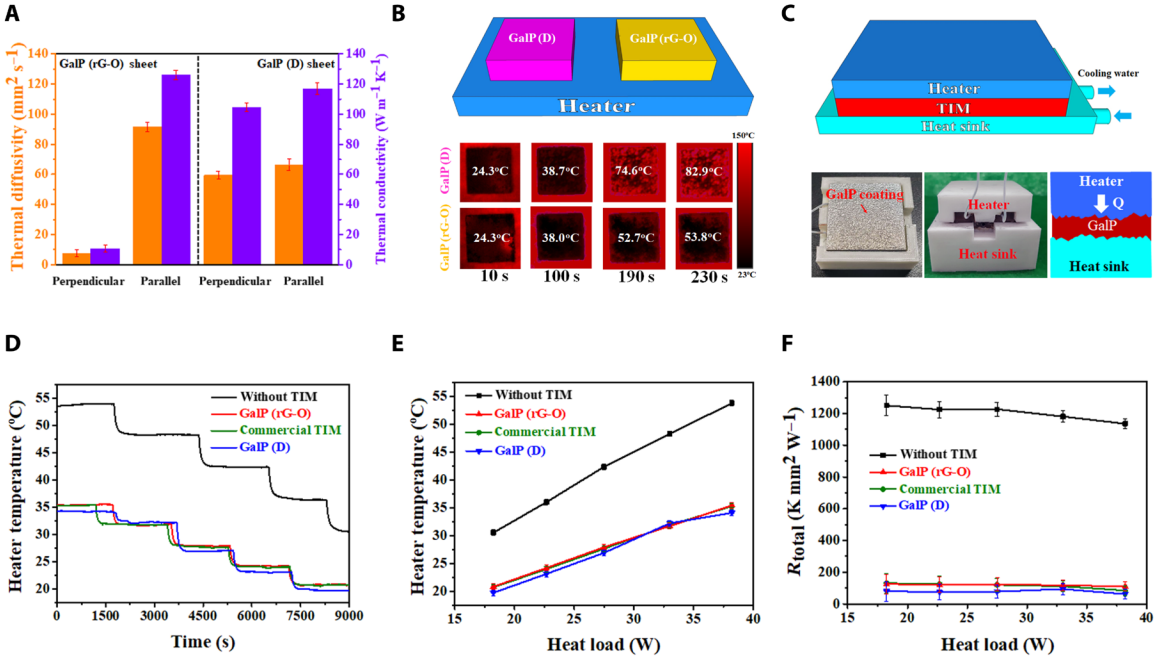

Fig. 4. Thermal performance of GaIP. (**A**) Thermal diffusivity and conductivity of GaIP (rG-O) and GaIP (D) parallel and perpendicular to the sheet. (**B**) Test system configuration for demonstrating the perpendicular heat transfer capability of two bulk GaIP (D) and GaIP (rG-O) blocks and the corresponding IR images of surface temperature changes. (**C**) Schematic of the GaIP TIM performance measurement system. (**D**) Temperature change of the stainless steel heater as a function of the heating time and (**E**) various powers at a steady state. (**F**) Total thermal resistance of GaIP samples. Photo credits: Chunhui Wang, Center for Multidimensional Carbon Materials, Institute for Basic Science.

with a thickness of 100 μm and a lateral size of 4.0 cm × 4.0 cm were placed between a heat source of variable power and a heat sink. For comparison, a commercial liquid metal thermal paste for a computer central processing unit (CPU) (Silver King, Thermalright, Taiwan; a published value for the thermal conductivity of this paste is 79 W m^{-1} K^{-1}; table S2) was used as a reference.

The heat source temperature rose rapidly when turned on, and when it had reached equilibrium, the temperature was recorded as a function of time. The heat source power was gradually reduced at fixed time intervals during the experiment. As shown in Fig. 4D, both GalP (D) and GalP (rG-O) showed effective cooling performance. The initial heat source temperature without a TIM was 53.6°C but was reduced to 35.3°C when GalP (rG-O) was used as the TIM, a reduction of 18.3°C. The commercial TIM showed the same performance, an 18.3°C reduction. In contrast to the thermal conductivity results, the smallest particle size GalP (D) composite (11 μm) had the best performance (fig. S26), a reduction of 19.5°C that exceeded the commercial TIM. We found that larger-sized diamond particles protrude from the bulk GalP (D), creating roughness and air gaps at the heat source and result in the decreased performance despite higher thermal conductivities.

On the basis of the linear variation of the steady heater temperature versus the power density (Fig. 4E), the equivalent heat transfer coefficients (equal to the reciprocal of the slope) of the heating system without TIM, with commercial TIM, GalP (rG-O), and GalP (D) are 0.83, 1.36, 1.36, and 1.43 W $°C^{-1}$, respectively, showing that the cooling efficiencies with GalP (D) and GalP (rG-O) as TIMs are respectively 1.7 and 1.6 times higher than without a TIM. The total thermal resistances R_{total} (Fig. 4F) for GalP (rG-O) and GalP (D) are far lower than that without a TIM and, for GalP (D), were better than the commercial gallium-based TIM. These data indicate that GalP has potential for use as a new material in thermal management.

We found a versatile method to fabricate nonmetallic/GLM composites that have paste or putty-like behavior. Various nonmetallic particles can mix with GLM in the presence of air to form GalP as long as the particle size is large enough, the volume percentage is high enough (but not too high), and the particle surface roughness is "low."

The properties of GalP are mainly determined by the filler. GalP (G-O) can be transformed into a Ga-based foam or converted to GalP (rG-O), which displayed very high EMI shielding performance. Both GalP (rG-O) and GalP (D) had excellent thermal properties, with GalP (D) exceeding the performance of a liquid Ga–based TIM. Our discovery of a methodology that can create GLM composites with a variety of different filler types greatly broadens the scope for functional GLM-based composites with a wide variety of functional fillers.

MATERIALS AND METHODS

Synthesis of GalP composites

GalP (G-O)

G-O powder was gradually added (in increments) to liquid Ga (heated to 40°C) in a Teflon beaker under vigorous mechanical stirring (HS-50A, Daihan Scientific Co.; 3000 rpm). When the G-O addition reached 1.8 wt %, the viscosity of the mixture was too high for mechanical stirring; at weight % loadings smaller than 1.8 wt %, the composite is not putty-like [it is either liquid-like (until about 1.6 wt %) or paste-like (1.6 to 1.8 wt %)]. Thus, the threshold loading needed to make GalP (G-O) was 1.8 wt %. The warm viscous paste-like mixture containing 1.8 wt % G-O was transferred with additional G-O gradually (again, in increments) added to an oscillating ball mill (Retsch, Germany; 1 Teflon ball, 12 mm in diameter) for further mixing at a frequency of 30 Hz at room temperature (we found that a maximum total of 8.0 wt % can form a stable putty phase). The ball milling generated enough heat to keep the paste-like mixture above 30°C. A soft GalP with a silver color containing 3.6 wt % G-O was removed from the mill for further study; the final step after reaching 3.6 wt % involved ball milling at 30 Hz for roughly 10 min to achieve a "uniform putty." Unless otherwise stated, in this work, GalP (G-O) has a composition of 3.6 wt %. (Note that mixing G-O with Ga only by mechanical stirring or oscillating ball mill makes no difference as far as can be told by eye. The approach described above, where we achieve 1.8 wt % with the mechanical mixer and then switch to the ball mill to reach, e.g., 3.6 wt %, was substantially faster. We found that generating the needed gallium oxide component with ball mill alone starting from 0.0 wt % was challenging.)

GalP (rG-O)

The above approach could not be used for synthesizing GalP (rG-O). Our attempts at stirring rG-O powder with liquid Ga did not result in intimate mixing, and two separate phases always remained. However, we found that directly heating GalP (G-O) in an inert atmosphere to thermally reduce G-O followed by mechanical grinding could yield a stable GalP (rG-O). In a typical experiment, GalP (G-O, 3.6 wt %) was heated to 700°C for 1 hour under flowing Ar. After cooling, a small amount of pure Ga was found to have separated from the putty phase. Grinding with a mortar and pestle (about 10 min) reincorporated the gallium and formed a stable GalP (rG-O). The rG-O mass loading in GalP (rG-O) is 1.6 wt %.

GalP (D), GalP (Gr), and GalP (SiC)

Micrometer-scale diamond (6.5 μm average particle size), graphite (180 μm average particle size), or silicon carbide (102 μm average particle size) powder was directly mixed with Ga in air with vigorous mechanical stirring to fabricate GalP (D), GalP (Gr), or GalP (SiC). Additional ball milling was not performed. The maximum weight % of each additive that could be incorporated was as follows: diamond, 32.2 wt %; graphite, 32.5 wt %; silicon carbide, 35.7 wt %. (Minimum and maximum weight percentage loadings in which the composite behaves like a putty are shown for various GalPs in fig. S17.)

Preparation of EGaIn, EGaSn, and EGaInSn (Galinstan)

EGaIn (75.0% Ga and 25.0% In by weight), EGaSn (92.0% Ga and 8.0% Sn by weight), and EGaInSn (Galinstan, 68.0% Ga, 22.0% In, and 10.0% Sn by weight) were prepared using methods reported in the literature. A quantity of gallium was heated and stirred to which the correct weights of indium, tin, or both were added to form the eutectic.

Preparation of eutectic putties

The preparation of eutectic-based putty composites was performed in an identical manner to pure GalPs described above but substituting the pure gallium with the eutectic.

Fabrication of macroscopic forms from GalP (G-O)

Rods or fibers

Rods or fibers were prepared using Teflon tubes as the mold. The sample thickness and length could be modified by selecting different tube sizes. In a typical experiment, GalP (G-O) was heated to

40°C and then drawn into a syringe from which it was expelled into the tube. The filled tube was cooled to −80°C, and the rod or fiber was removed by cutting away the tube.

Plates or films

Plates or films were prepared by the doctor-blade method. Because of the high viscosity of GalPs, they were spread over the entire substrate surface by a blade before using the doctor-blade apparatus. In a typical experiment, GalP (G-O) was heated to about 40°C and a small quantity was then spread thinly over a Teflon plate by a stainless steel blade. A doctor-blade apparatus with a fixed gap size was then used to create a uniform thickness over the whole substrate area. The coated substrate was then placed in a low-temperature freezer (−80°C) for ~1 min. The film (or plate) could then be easily separated from the Teflon substrate.

Bulk materials or blocks

Silicone rubber with a 12.4-mm-diameter hole was used as a mold to fabricate a cylinder of bulk GalP (G-O). The mold was filled with viscous GalP (G-O) by hand and transferred to a freezer (−80°C) for 10 min. The solidified GalP (G-O) cylinder could be easily removed from the mold. In general, any shape could be prepared using this technique. Note that the fabrication of GalP (rG-O), GalP (D), GalP (Gr), or GalP (SiC) macroscopic materials was performed in an identical manner to GalP (G-O) described above.

Preparation of electromagnetic shielding testing samples

Commercial A4 paper (Samsung C&T; 75.0 g m^{-2}) or an rG-O film (17.2 μm thick, prepared by evaporating a G-O dispersion in a Teflon petri dish in air for 2 days and then reducing it by immersion in a 57.0 wt % HI aqueous solution at 85°C for 1 hour) was coated with GalP (rG-O) by a doctor blade following the coating procedure outlined above for plates or films. The film assembly was cut to a 22.86 mm × 10.16 mm rectangle. Electromagnetic shielding performance was measured using an Agilent PNA-X microwave network analyzer (N5242A).

EMI SE was used to measure the ability of the material to attenuate the electromagnetic wave strength, which is defined as the logarithm of incoming power (P_i) to transmitted power (P_t) of an electromagnetic wave in decibels

$$SE_{total} = 10\log\left(\frac{P_i}{P_t}\right) \quad (1)$$

When an electromagnetic wave propagates through a shielding material, the reflection (R), absorption (A), and transmission (T) must add up to 1, that is

$$R + A + T = 1 \quad (2)$$

The reflection (R) and transmission (T) coefficients were obtained from the network analyzer in the form of scattering parameters, "S_{mn}," which measure how energy is scattered from a material or device. The first letter "m" designates the network analyzer port receiving the EMI radiation, and the second letter "n" represents the port that is transmitting the incident energy. Vector network analyzer directly gives the output in the form of four scattering parameters (S_{11}, S_{12}, S_{21}, and S_{22}), which can be used to find the R and T coefficients as

$$R = |S_{11}|^2 = |S_{22}|^2 \quad (3)$$

$$T = |S_{12}|^2 = |S_{21}|^2 \quad (4)$$

The total EMI SE (EMI SE_T) is the sum of the contributions from reflection (SE_R), absorption (SE_A), and multiple internal reflections (SE_M). At higher EMI SE values, and with a multilayer EMI shield (as in the case of the few-layer graphene foam), multi-reflected waves get absorbed or dissipated as heat in the same way as the absorption mechanism. SE_{total} can be written as

$$SE_{total} = SE_R + SE_A \quad (5)$$

SE_R and SE_A can be expressed in terms of reflection and effective absorption considering the power of the incident electromagnetic waves inside the shielding material as

$$SE_R = 10\log\left(\frac{1}{1-R}\right) = 10\log\left(\frac{1}{1-|S_{11}|^2}\right) \quad (6)$$

$$SE_A = 10\log\left(\frac{1-R}{T}\right) = 10\log\left(\frac{1-|S_{11}|^2}{|S_{21}|^2}\right) \quad (7)$$

$$SE_{total} = 10\log\left(\frac{1}{|S_{21}|^2}\right) \quad (8)$$

Specific shielding effectiveness

SSE (dB cm^3 g^{-1}) is derived to compare the effectiveness of shielding materials (SE_{total}) taking into account the density (ρ), and thus, it can be obtained as follows

$$SSE = \frac{SE_{total}}{\rho} \quad (9)$$

SSE has a basic limitation, that is, it does not account for the thickness information. Higher values of SSE can be obtained at large thickness while maintaining a low density. However, large thickness increases the net weight and is disadvantageous. To account for the thickness contribution (t; cm), the following equation is used to evaluate the absolute effectiveness (SSE_t; dB cm^2 g^{-1}) of a material in relative terms

$$SSE_t = \frac{SSE}{t} \quad (10)$$

Calculation of EMI shielding efficiency (%)

EMI shielding efficiency represents the materials ability to block waves in terms of percentage. For example, EMI shielding efficiency of 10 dB corresponds to 90% blockage of incident radiation, and 30 dB corresponds to 99.9% blockage of incident radiation. EMI SE (dB) is converted into EMI shielding efficiency (%) using the equation as

$$\text{EMI shielding efficiency (\%)} = 100 - \left(\frac{1}{10^{\frac{SE_{total}}{10}}}\right) \times 100 \quad (11)$$

Characterization

An FEI Verios 460 SEM and a JEM-2100 TEM were used to examine the morphology of the samples. TEM specimens were prepared by focused ion beam milling using a Helios NanoLab 450HP. X-ray diffraction (XRD) patterns were acquired on a Rigaku SmartLab powder x-ray diffractometer using Cu Kα radiation and analyzed using MDI Jade software. A contact angle analyzer (Phoenix-I, South Korea) was used to measure the contact angle. Raman spectra (WiTec micro-Raman) were acquired with 532-nm laser excitation under ambient conditions. X-ray photoelectron spectroscopy was performed on

ESCALAB 250Xi (Thermo Fisher Scientific). An Instron 5982 was used to measure the compressive and tensile strengths. All the samples were tested at 26°C. The specific heat capacity (C_p) of the samples were evaluated using differential scanning calorimetry on a Q200 (TA instruments, USA). A thermal conductivity of the samples was measured with an LFA 467 NanoFlash apparatus (Netzsch, Germany). IR photographs were captured using an FLIR a325sc (USA). TGA-MS was measured by a TA Instruments Q500 with the evolved gas analyzed by a HIDEN QGA system. The viscoelastic behavior of the GalP samples was obtained with a rotating parallel-plate rheometer (Discovery Hybrid Rheometer HR-2, TA Instruments).

SUPPLEMENTARY MATERIALS

Supplementary material for this article is available at http://advances.sciencemag.org/cgi/content/full/7/1/eabe3767/DC1

REFERENCES AND NOTES

1. J. J. Yan, Y. Lu, G. J. Chen, M. Yang, Z. Gu, Advances in liquid metals for biomedical applications. *Chem. Soc. Rev.* **47**, 2518–2533 (2018).
2. T. Daeneke, K. Khoshmanesh, N. Mahmood, I. A. de Castro, D. Esrafilzadeh, S. J. Barro, M. D. Dickey, K. Kalantar-zadeh, Liquid metals: Fundamentals and applications in chemistry. *Chem. Soc. Rev.* **47**, 4073–4111 (2018).
3. K. Kalantar-Zadeh, J. B. Tang, T. Daeneke, A. P. O'Mullane, L. A. Stewart, J. Liu, C. Majidi, R. S. Ruoff, P. S. Weiss, M. D. Dickey, Emergence of liquid metals in nanotechnology. *ACS Nano* **13**, 7388–7395 (2019).
4. Q. Wang, Y. Yu, J. Liu, Preparations, characteristics and applications of the functional liquid metal materials. *Adv. Eng. Mater.* **20**, 1700781 (2018).
5. M. D. Dickey, R. C. Chiechi, R. J. Larsen, E. A. Weiss, D. A. Weitz, G. M. Whitesides, Eutectic gallium-indium (EGaIn): A liquid metal alloy for the formation of stable structures in microchannels at room temperature. *Adv. Funct. Mater.* **18**, 1097–1104 (2008).
6. M. F. Dumke, T. A. Tombrello, R. A. Weller, R. M. Housley, E. H. Cirlin, Sputtering of the gallium-indium eutectic alloy in the liquid phase. *Surf. Sci.* **124**, 407–422 (1983).
7. T. Liu, P. Sen, C. C. J. Kim, Characterization of nontoxic liquid-metal alloy galinstan for applications in microdevices. *J. Microelectromech. Syst.* **21**, 443–450 (2012).
8. R. Guo, X. L. Wang, H. Chang, W. Z. Yu, S. T. Liang, W. Rao, J. Liu, Ni-GaIn amalgams enabled rapid and customizable fabrication of wearable and wireless healthcare electronics. *Adv. Eng. Mater.* **20**, 1800054 (2018).
9. C. F. Pan, E. J. Markvicka, M. H. Malakooti, J. J. Yan, L. M. Hu, K. Matyjaszewski, C. Majidi, A liquid-metal-elastomer nanocomposite for stretchable dielectric materials. *Adv. Mater.* **31**, 1900663 (2019).
10. S. Liu, M. C. Yuen, E. L. White, J. W. Boley, B. Deng, G. J. Cheng, R. Kramer-Bottiglio, Laser sintering of liquid metal nanoparticles for scalable manufacturing of soft and flexible electronics. *ACS Appl. Mater. Interfaces* **10**, 28232–28241 (2018).
11. X. K. Li, M. J. Li, L. Zong, X. C. Wu, J. You, P. K. Du, C. X. Li, Liquid metal droplets wrapped with polysaccharide microgel as biocompatible aqueous ink for flexible conductive devices. *Adv. Funct. Mater.* **28**, 1804197 (2018).
12. M. D. Bartlett, N. Kazem, M. J. Powell-Palm, X. N. Huang, W. H. Sun, J. A. Malen, C. Majidi, High thermal conductivity in soft elastomers with elongated liquid metal inclusions. *Proc. Natl. Acad. Sci. U.S.A.* **114**, 2143–2148 (2017).
13. I. D. Joshipura, H. R. Ayers, C. Majidi, M. D. Dickey, Methods to pattern liquid metals. *J. Mater. Chem. C* **3**, 3834 (2015).
14. W. Kong, Z. Y. Wang, M. Wang, K. C. Manning, A. Uppal, M. D. Green, R. Y. Wang, K. Rykaczewski, Oxide-mediated formation of chemically stable tungsten-liquid metal mixtures for enhanced thermal interfaces. *Adv. Mater.* **31**, 1904309 (2019).
15. J. Tang, X. Zhao, J. Li, R. Guo, Y. Zhou, J. Liu, Gallium-based liquid metal amalgams: Transitional-state metallic mixtures (TransM2ixes) with enhanced and tunable electrical, thermal, and mechanical properties. *ACS Appl. Mater. Interfaces* **9**, 35977–35987 (2017).
16. M. Tavakoli, M. H. Malakooti, H. Paisana, Y. Ohm, D. G. Marques, P. A. Lopes, A. P. Piedade, A. T. Almeida, C. Majidi, EGaIn-assisted room-temperature sintering of silver nanoparticles for stretchable, inkjet-printed, thin-film electronics. *Adv. Mater.* **30**, 1801852 (2018).
17. A. L. Lereu, F. Lemarchand, M. Zerra, M. Yazdanpanah, A. Passian, Optical properties and plasmonic response of silver-gallium nanostructures. *J. Appl. Phys.* **117**, 063110 (2015).
18. X. Wang, W. Yao, R. Guo, X. Yang, J. Tang, J. Zhang, W. P. Gao, V. Timchenko, J. Liu, Soft and moldable Mg-doped liquid metal for conformable skin tumor photothermal therapy. *Adv. Healthc. Mater.* **7**, 1800318 (2018).
19. X. Huang, X. Y. Qi, F. Boey, H. Zhang, Graphene-based composites. *Chem. Soc. Rev.* **41**, 666–686 (2012).
20. A. P. Yu, P. Ramesh, M. E. Itkis, E. Bekyarova, R. C. Haddon, Graphite nanoplatelet–epoxy composite thermal interface materials. *J. Phys. Chem. C* **111**, 7565–7569 (2007).
21. E. A. Ekimov, N. V. Suetin, A. F. Popovich, V. G. Ralchenko, Thermal conductivity of diamond composites sintered under high pressures. *Diam. Relat. Mater.* **17**, 838–843 (2008).
22. L. L. Snead, R. H. Jones, A. Kohyama, P. Fenici, Status of silicon carbide composites for fusion. *J. Nucl. Mater.* **233**, 26–36 (1996).
23. E. T. Thostenson, T. W. Chou, Processing-structure-multi-functional property relationship in carbon nanotube/epoxy composites. *Carbon* **44**, 3022–3029 (2006).
24. Y.-G. Park, H. Min, H. Kim, A. Zhexembekova, C. Y. Lee, J.-U. Park, Three-dimensional, high-resolution printing of carbon nanotube/liquid metal composites with mechanical and electrical reinforcement. *Nano Lett.* **19**, 4866–4872 (2019).
25. L. Y. Zhao, S. Chu, X. C. Chen, G. Chu, Efficient heat conducting liquid metal/CNT pads with thermal interface materials. *Bull. Mater. Sci.* **42**, 192 (2019).
26. V. Kamysbayev, N. M. James, A. S. Filatov, V. Srivastava, B. Anasori, H. M. Jaeger, Y. Gogotsi, D. V. Talapin, Colloidal gelation in liquid metals enables functional nanocomposites of 2D metal carbides (MXenes) and lightweight metals. *ACS Nano* **13**, 12415–12424 (2019).
27. S. Wei, Z. F. Yu, L. J. Zhou, J. D. Guo, Investigation on enhancing the thermal conductance of gallium-based thermal interface materials using chromium-coated diamond particles. *J. Mater. Sci. Mater. Electron.* **30**, 7194–7202 (2019).
28. B. Konkena, S. Vasudevan, Understanding aqueous dispersibility of graphene oxide and reduced graphene oxide through pKa measurements. *J. Phys. Chem. Lett.* **3**, 867–872 (2012).
29. İ. Mutlay, L. B. Tudoran, Percolation behavior of electrically conductive graphene nanoplatelets/polymer nanocomposites: Theory and experiment. *Fuller. Nanotub. Carbon Nanostructures* **22**, 413–433 (2014).
30. A. Plech, U. Klemradt, H. Metzger, J. Peisl, In situ X-ray reflectivity study of the oxidation kinetics of liquid gallium and the liquid alloy $Ga_{0.93}Hg_{0.07}$. *J. Phys. Condens. Matter* **10**, 971–982 (1998).
31. M. D. Dickey, Emerging applications of liquid metals featuring surface oxides. *ACS Appl. Mater. Interfaces* **6**, 18369–18379 (2014).
32. J. Cutinho, B. S. Chang, S. Oyola-Reynoso, J. Chen, S. S. Akhter, I. D. Tevis, N. J. Bello, A. Martin, M. C. Foster, M. M. Thuo, Autonomous thermal-oxidative composition inversion and texture tuning of liquid metal surfaces. *ACS Nano* **12**, 4744–4753 (2018).
33. S. Liu, S. N. Reed, M. J. Higgins, M. S. Titus, R. Kramer-Bottiglio, Oxide rupture-induced conductivity in liquid metal nanoparticles by laser and thermal sintering. *Nanoscale* **11**, 17615–17629 (2019).
34. R. C. Chiechi, E. A. Weiss, M. D. Dickey, G. M. Whitesides, Eutectic gallium-indium (EGaIn): A moldable liquid metal for electrical characterization of self-assembled monolayers. *Angew. Chem. Int. Ed.* **47**, 142–144 (2008).
35. R. J. Larsen, M. D. Dickey, G. M. Whitesides, D. A. Weitz, Viscoelastic properties of oxide-coated liquid metals. *J. Rheol.* **53**, 1305–1326 (2009).
36. M. R. Khan, C. B. Eaker, E. F. Bowden, M. D. Dickey, Giant and switchable surface activity of liquid metal via surface oxidation. *Proc. Natl. Acad. Sci. U.S.A.* **30**, 14047–14051 (2014).
37. C. J. Zhang, Q. Yang, C. Shan, J. Z. Zhang, J. L. Yong, Y. Fang, X. Hou, F. Chen, Tuning a surface super-repellent to liquid metal by a femtosecond laser. *RSC Adv.* **10**, 3301–3306 (2020).
38. S. S. Kadlaskar, J. H. Yoo, Abhijeet, J. B. L. , W. J. Choi, Cost-effective surface modification for Galinstan lyophobicity. *J. Colloid Interface Sci.* **492**, 33–40 (2017).
39. Z. Y. Chen, J. B. Lee, Surface modification with Gallium coating as nonwetting surfaces for Gallium-based liquid metal droplet manipulation. *ACS Appl. Mater. Interfaces* **11**, 35488–35495 (2019).
40. C. Ladd, J. H. So, J. Muth, M. D. Dickey, 3D printing of free standing liquid metal microstructures. *Adv. Mater.* **25**, 5081–5085 (2013).
41. A. R. Jacob, D. P. Parekh, M. D. Dickey, L. C. Hsiao, Interfacial rheology of gallium-based liquid metals. *Langmuir* **35**, 11774–11783 (2019).
42. M. M. Ruedaa, M.-C. Auscher, R. Fulchiron, T. Périé, G. Martin, P. Sonntag, P. Cassagnau, Rheology and applications of highly filled polymers: A review of current understanding. *Prog. Polym. Sci.* **66**, 22–53 (2017).
43. Y. Qiu, F. Guo, R. Hurt, I. Külaots, Explosive thermal reduction of graphene oxide-based materials: Mechanism and safety implications. *Carbon* **72**, 215–223 (2014).
44. D. Townsend, S. Parry, N. K. Bourne, P. J. Withers, D. C. Wood, G. J. Appleby-Thomas, A. Hameed, On the compression of aluminum foam structures under shock. *AIP Conf. Proc.* **1793**, 110010 (2017).
45. M. K. Zhang, P. J. Zhang, Q. Wang, L. Li, S. J. Dong, J. Liu, W. Rao, Stretchable liquid metal electromagnetic interference shielding coating materials with superior effectiveness. *J. Mater. Chem. C* **7**, 10331–10337 (2019).

46. F. Shahzad, M. Alhabeb, C. B. Hatter, B. Anasori, S. M. Hong, C. M. Koo, Y. Gogotsi, Electromagnetic interference shielding with 2D transition metal carbides (MXenes). *Science* **353**, 1137–1140 (2016).
47. D. P. H. Hasselman, K. Y. Donaldson, J. Liu, L. J. Gauckler, P. D. Ownby, Thermal conductivity of a particulate-diamond-reinforced cordierite matrix composite. *J. Am. Ceram. Soc.* **77**, 1757–1760 (1994).
48. S.-H. Joo, D.-H. Pi, A. D. H. Setyawan, H. Kato, M. Janecek, Y. C. Kim, S. Lee, H. S. Kim, Work-hardening induced tensile ductility of bulk metallic glasses via high-pressure torsion. *Sci. Rep.* **5**, 9660 (2015).
49. J. N. Hohman, M. H. Kim, G. A. Wadsworth, H. R. Bednar, J. Jiang, M. A. LeThai, P. S. Weiss, Directing substrate morphology via self-assembly: Ligand-mediated scission of gallium-indium microspheres to the nanoscale. *Nano Lett.* **11**, 5104–5110 (2011).
50. C. V. Ramana, E. J. Rubio, C. D. Barraza, A. M. Gallardo, S. McPeak, S. Kotru, J. T. Grant, Chemical bonding, optical constants, and electrical resistivity of sputter-deposited gallium oxide thin films. *J. Appl. Phys.* **115**, 043508 (2014).
51. R. Al-Gaashani, A. Najjar, Y. Zakaria, S. Mansour, M. A. Atieh, XPS and structural studies of high quality graphene oxide and reduced graphene oxide prepared by different chemical oxidation methods. *Ceram. Int.* **45**, 14439–14448 (2019).
52. X. P. Shui, D. D. L. Chung, Nickel filament polymer-matrix composites with low surface impedance and high electromagnetic interference shielding effectiveness. *J. Electron. Mater.* **26**, 928–934 (1997).
53. H. Ji, R. Zhao, N. Zhang, C. X. Jin, X. F. Lu, C. Wang, Lightweight and flexible electrospun polymer nanofiber/metal nanoparticle hybrid membrane for high-performance electromagnetic interference shielding. *NPG ASIA Mater.* **10**, 749–760 (2018).
54. B. Shen, W. T. Zhai, W. G. Zheng, Ultrathin flexible graphene film: An excellent thermal conducting material with efficient EMI shielding. *Adv. Funct. Mater.* **24**, 4542–4548 (2014).
55. J. Ling, W. Zhai, W. Feng, B. Shen, J. Zhang, W. g. Zheng, Facile preparation of lightweight microcellular polyetherimide/graphene composite foams for electromagnetic interference shielding. *ACS Appl. Mater. Interfaces* **5**, 2677–2684 (2013).
56. B. Shen, Y. Li, W. T. Zhai, W. G. Zheng, Compressible graphene-coated polymer foams with ultralow density for adjustable electromagnetic interference (EMI) shielding. *ACS Appl. Mater. Interfaces* **8**, 8050–8057 (2016).
57. Y. Li, X. L. Pei, B. Shen, W. T. Zhai, L. H. Zhang, W. G. Zheng, Polyimide/graphene composite foam sheets with ultrahigh thermostability for electromagnetic interference shielding. *RSC Adv.* **5**, 24342–24351 (2015).

Acknowledgments: We thank K. Kalantar-Zadeh for comments and suggestions on an earlier version of this manuscript, first submitted for peer-review on September 11, 2019. S. Y. Kim and S. M. Oh for discussion and suggestions on rheology testing, G. Byun and T. H.-Y. Nguyen for allowing us to use their Agilent PNA-X system to measure the EMI response, and S. H. Lee for helpful comments about diamond powders. We also thank M. Wang, Y. Li, Y. Jiang, and L. Zhang for help. **Funding:** This work was supported by IBS-R019-D1. **Author contributions:** R.S.R. conceived and supervised the research project. C.W. conducted the experiments and found various aspects while making many of the materials described. Y.G. worked closely with C.W. in the early stages; together, they first made GalP and Y.G. provided helpful suggestions and did the Raman measurements. B.V.C. and R.S.R. provided scientific insights about the formation and range of stability of the putty-like materials (e.g., dependence on fraction of filler and other factors). S.L. and J.L. did the thermal management testing. Q.L. did the EMI shielding measurements. S.R.J. and G.-H.K. did the thermal conductivity measurements. O.B. did the TGA-MS characterization. H.Z. did the XRD characterization. W.K.S. did the TEM characterization. M.H. did the x-ray photoelectron spectroscopy measurements. M.W. and C.W. made the molds for sample preparation. C.W., R.S.R., and B.V.C. wrote the manuscript. All coauthors revised and commented on the manuscript. **Competing interests:** The Institute for Basic Science (IBS) and Ulsan National Institute of Science and Technology (UNIST), along with their researchers (R.S.R., C.W., and Y.G.), have filed a patent application related to the technology and intellectual property reported here (no. KR 10-2020-0146055, filed on 4 November 2020, title: A general approach to composites containing non-metallic fillers and liquid gallium). If licensing or commercialization occurs, R.S.R., C.W., and Y.G. are entitled to standard royalties. The authors declare no other competing interests. **Data and materials availability:** All data needed to evaluate the conclusions in the paper are present in the paper and/or the Supplementary Materials. Additional data related to this paper may be requested from the authors.

Submitted 18 August 2020
Accepted 6 November 2020
Published 1 January 2021
10.1126/sciadv.abe3767

Citation: C. Wang, Y. Gong, B. V. Cunning, S. Lee, Q. Le, S. R. Joshi, O. Buyukcakir, H. Zhang, W. K. Seong, M. Huang, M. Wang, J. Lee, G.-H. Kim, R. S. Ruoff, A general approach to composites containing nonmetallic fillers and liquid gallium. *Sci. Adv.* **7**, eabe3767 (2021).

A general approach to composites containing nonmetallic fillers and liquid gallium

Chunhui Wang, Yan Gong, Benjamin V. Cunning, Seunghwan Lee, Quan Le, Shalik R. Joshi, Onur Buyukcakir, Hanyang Zhang, Won Kyung Seong, Ming Huang, Meihui Wang, Jaeseon Lee, Gun-Ho Kim and Rodney S. Ruoff

Sci Adv **7** (1), eabe3767.
DOI: 10.1126/sciadv.abe3767